Available online at www.sciencedirect.com
ScienceDirect
Trans. Nonferrous Met. Soc. China 29(2019) 448−459
Transactions of Nonferrous Metals Society of China
www.tnmsc.cn

Modification of constitutive model and evolution of activation energy on 2219 aluminum alloy during warm deformation process

Lei LIU[1,2,3], Yun-xin WU[1,2,3], Hai GONG[1,2,3], Kai WANG [1,2,3]

1. Light Alloy Research Institute, Central South University, Changsha 410083, China;
2. Collaborative Innovation Center of Advanced Nonferrous Structural Materials and Manufacturing, Central South University, Changsha 410083, China;
3. State Key Laboratory of High Performance Complex Manufacturing, Central South University, Changsha 410083, China

Received 7 January 2018; accepted 19 June 2018

Abstract: To investigate the flow behavior of 2219 Al alloy during warm deformation, the thermal compression test was conducted in the temperature range of 483−573 K and the strain rate range of 0.001−5 s^{-1} on a Gleeble−3500 thermomechanical simulation unit. The true stress−true strain curves obtained showed that the flow stress increased with the decrease in temperature and/or the increase in strain rate and the softening mechanism primarily proceeded via dynamic recovery. The modification on the conventional Arrhenius-type constitutive model approach was made, the material variables and activation energy were determined to be dependent on the deformation parameters. The modified flow stresses were found to be in close agreement with the experimental values. Furthermore, the activation energy obtained under different deformation conditions showed that it decreased with the rise in temperature and/or strain rate, and was also affected by the coupled effect of strain and strain rate.

Key words: 2219 Al alloy; warm deformation; flow behavior; constitutive model; activation energy

1 Introduction

2219 Al alloy (i.e. Al−Cu−Mn alloy), as one of Al alloys that can be strengthened by heat treatment, has very good mechanical properties like high heat resistance, good weldability, and high strength [1]. Thus, it has been widely applied in the manufacturing of structures and components in aerospace industry [2−4]. During the forming process of a certain component, required mechanical properties and microstructures can be obtained by setting appropriate deformation parameters such as temperature, strain rate and strain [5]. Therefore, it is essential to determine the flow properties of 2219 Al alloy under different deformation conditions during the forming process.

The constitutive model is a mathematical relationship established between the flow properties of the material and deformation parameters [6]. Many efforts [7−20] have been made in developing the accurate constitutive model. The hyperbolic sine model, as one of the widely used phenomenological model, has been successfully constructed and used to predict the flow properties of various materials. SELLARS and MCTEGART [7] firstly proposed a hyperbolic sine model with Z parameter to describe the flow behavior of the material. Also, CEPEDA−JIMÉNEZ et al [8] established the constitutive model of 2024 Al-T351 alloy using the Arrhenius-type model. However, one major disadvantage of this model is that the effect of strain was not considered [9]. Then, the modified sine hyperbolic model considering strain compensation approach (SCA) was put forward to enhance the prediction accuracy of the model, and the method has been widely used in 42CrMo steel [10], H62 brass [11], IMI834 titanium alloy [12,13] and Al alloy [14,15]. LIN et al [16−18] have established many effective constitutive models for different metals and alloys, such as a physically-based constitutive model considering dislocation density for a typical nickel-based superalloy [16], a revised Johnson−

Foundation item: Projects (U1637601, 51405520, 51327902) supported by the National Natural Science Foundation of China; Project (ZZYJKT2017-06) supported by State Key Laboratory of High Performance Complex Manufacturing of Central South University, China
Corresponding author: Hai GONG; Tel: +86-18890355864; E-mail: CSU2019@163.com
DOI: 10.1016/S1003-6326(19)64954-X

Cook model for Al−Cu−Mg alloy [17] and Al−Zn−Mg−Cu alloy [18] by modifying the material parameters. In addition, QUAN et al [19−21] mainly focused on the comparison between the improved Arrhenius-type constitutive models by SCA and artificial neural network models for 20MnNiMo alloy [19], 7050 Al alloy [20] and Ti−6Al−2Zr−1Mo−1V alloy [21]. Basically, all the models above agree that the activation energy is a constant under different deformation conditions or just strain dependent. However, many scholars [22−24] have criticized this idea and thought that activation energy can be influenced by temperature and applied stress. However, the influence of deformation parameters on material parameters and activation energy is rarely considered.

Recently, intermediate thermo-mechanical treatment (ITMT) has been applied to improving the grain refining, the strength and the plasticity during material forming process [25]. WARD et al [26] used this method to refine grain size of the 7050 Al alloy plate to 30 μm in length and 15 μm in width, and the elongation rate in the width of the plate increased by 52%. Warm deformation is adopted in ITMT process to obtain adequate storage energy for further static recrystallization. Therefore, it is of great significance and necessity to investigate the flow properties of 2219 Al alloy during warm deformation for ITMT. Some studies focused on the flow behavior of 5000 and 6000 series Al alloys during warm deformation [27,28]. However, the study of the constitutive model of 2219 Al alloy under warm deformation was rarely reported.

In this work, the flow properties of 2219 Al alloy at different temperatures and strain rates were studied based on a thermal compression test. By considering the temperature compensation, the modified hyperbolic sine model was established on deformation parameters. The evolution of activation energy was described under different deformation conditions as well.

2 Experimental

The 2219 Al alloy was subjected to the thermal compression test, and its chemical composition is shown in Table 1. The samples were taken from hot-rolled plates and were machined according to the shape of Rastegaev sample. The schematic diagram and the picture of the real sample are shown in Fig. 1. This sample is characterized by shallow grooves at both ends filled with lubricants (graphite and lubrication oil). During deformation, the lubricant in the closed cavity can reduce the friction between the sample and the mold. A uniaxial thermal compression test was conducted on the Gleeble−3500 thermomechanical simulation unit.

For the actual industrial production, the temperature range of 2219 Al alloy during warm deformation is 500−550 K, and the strain rate in the processing is less than 5 s^{-1}. Therefore, in this experiment, the samples were deformed in a moderate temperature range of 483−573 K and strain rates range of 0.001−5 s^{-1} to the maximum strain of 0.8. Before the compression, the samples were firstly heated to deformation temperature at a speed of 5 K/s for 3 min. The samples were then deformed under a constant strain rate to the maximum strain of 0.8, and then immediately water quenched to preserve the deformed microstructure. The curve of the compression process is shown in Fig. 2. Temperature, displacement, speed and other conditions were numerically controlled from the computer system, and the true stress−true strain data were collected.

Table 1 Chemical composition of 2219 Al alloy (mass fraction, %)

Cu	Mn	Si	Zr	Fe
5.8−6.8	0.2−0.4	≤ 0.2	0.1−0.25	≤0.3
Mg	Zn	V	Ti	Al
≤ 0.02	0.10	0.05−0.15	0.02−0.1	Bal.

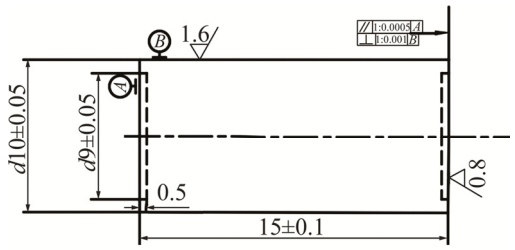

(a)

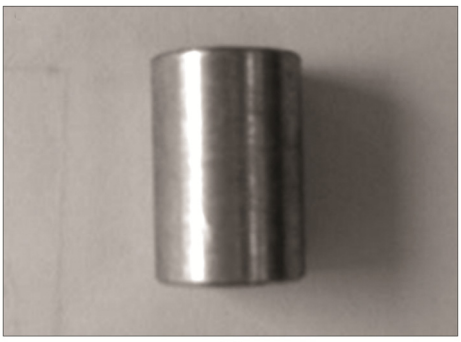

(b)

Fig. 1 Schematic diagram of thermal compression specimen (a) and picture of real sample (b)

3 Results and discussion

3.1 Flow behavior

A lot of energy will be consumed for metals and alloys during plastic deformation, a small part of which is kept in the form of storage energy, and most of which

is converted to heat energy [29]. Under low strain rate (<1 s^{-1}), the deformation time is relatively long. Thus, it can be approximately considered as isothermal deformation process by heat dissipation and equipment compensation. However, the deformation time is much shorter under high strain rate (>1 s^{-1}), which makes that the heat energy generated by the deformation energy will not dissipate in time. Therefore, the temperature of sample rises sharply and the true stress−true strain data obtained from thermal compression test are influenced by the temperature rise [30]. The temperature variation under different strain rates of the whole process is collected from the computer, as shown in Fig. 3.

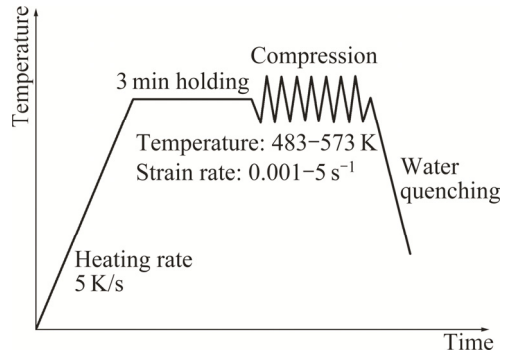

Fig. 2 Thermal simulation process curve

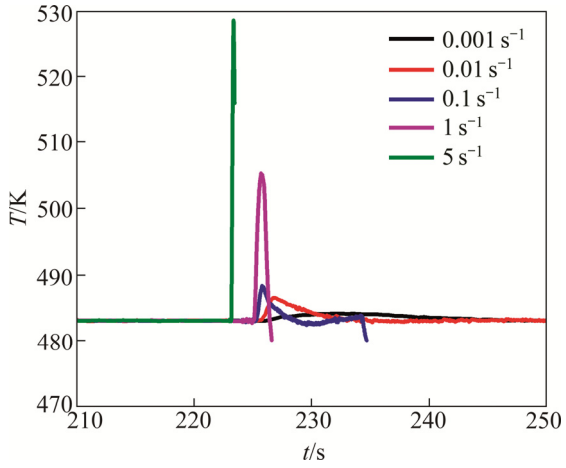

Fig. 3 Temperature variation of whole compression process with time under different strain rates

From Fig. 3, it can be observed that the temperature rises with the increase in strain rate during the compression process. Moreover, the temperature rise is higher than 5 K under the strain rates of 1 and 5 s^{-1}; however, the overall temperature rise is negligible at the strain rate of 0.001−0.1 s^{-1}. Temperature rise that occurs within the samples due to rapid plastic deformation may lead to flow softening, and a correction should be applied to the data obtained to account for this [31]. The magnitude of the associated softening ($\Delta\sigma$) caused by temperature rise can be estimated from the following formula described by Baragar [32]:

$$\Delta\sigma = \frac{Q}{n\alpha R}\left(\frac{1}{T_{\text{selected}}} - \frac{1}{T_{\text{real}}}\right) \quad (1)$$

where Q is the activation energy (J/mol), n and α are material parameters, R is the mole gas constant (J/(mol·K^{-1})), T_{selected} is the selected temperature (K), and T_{real} is the measured temperature (K).

According to Eq. (1), the true stress values under the strain rate of 1 and 5 s^{-1} are corrected, and all the true stress−true strain curves are shown in Fig. 4. It can be observed that the modified stress is greater than the experimental value. Therefore, the temperature rise is one of the most important factors for the flow softening of the material in the rapid deformation process.

It can be seen from Fig. 4 that flow stress is very sensitive to strain rate and temperature. Moreover, the flow stress usually increases with the decrease in temperature or increase in strain rate. In the whole compression process, the flow stress increases rapidly at the initial stage, and then remains stable or slightly decreases after peak stress reaches. This is because the strain is relatively small and the distribution of dislocation in grains is also relatively homogeneous in the initial stage. With the increase in deformation, the dislocation density is higher, and the dislocation movement is becoming more difficult, which makes the stress increase dramatically. With the rise in dislocation density, the dislocation in the grain and at grain boundary can be reorganized due to slip and climb, so the dislocation density is reduced and the alloy is softened. The equilibrium between work hardening and dynamic softening makes the flow stress almost constant. In general, the dynamic recovery keeps the flow stress curves to be straight while the dynamic recrystallization causes them to decrease [33]. Therefore, the softening mechanism of 2219 Al alloy during warm deformation is mainly dynamic recovery.

Also, it can also be observed that the flow stress decreases with the increase in the temperature under the same strain rate. This is because the increase in temperature makes the thermal activation effect strengthened, the kinetic energy of the atoms increased, and the critical shear stress of the atoms decreased in the deformation process. Moreover, the increase in temperature leads to the rearrangement of the dislocation, which is favorable for the reduction of dislocation density. Thus, the stress level of the alloy is decreased. On the other hand, the flow stress rises as the strain rate increases at the same temperature because the deformation time decreases when the strain rate is high, which makes the dynamic recovery process incomplete, so the flow stress will increase. This also indicates that 2219 Al alloy is sensitive to the positive strain rate.

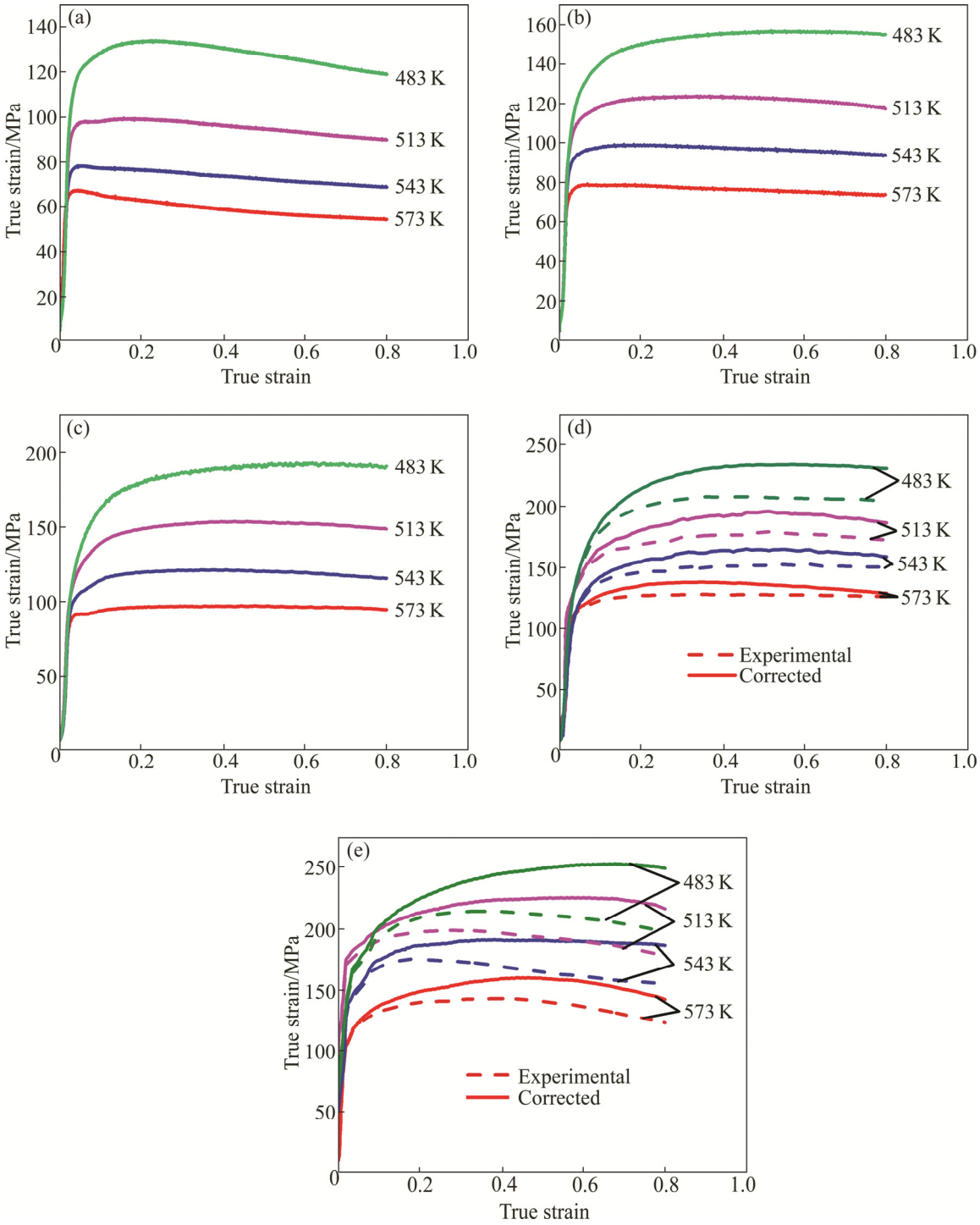

Fig. 4 True stress−true strain curves of experimental 2219 Al alloy under different temperatures and strain rates: (a) 0.001 s^{-1}; (b) 0.01 s^{-1}; (c) 0.1 s^{-1}; (d) 1 s^{-1}; (e) 5 s^{-1}

3.2 Modeling of constitutive equation by SCA

The true stress−true strain data obtained by the unidirectional thermal compression test can be used to determine the material parameters in the constitutive equation [34]. The relationship between flow stress and deformation parameters is usually expressed by the Arrhennius equation containing Z parameter and can be mathematically expressed as follows:

$$Z = \dot{\varepsilon}\exp(\frac{Q}{RT}) = Af(\sigma) \tag{2}$$

$$f(\sigma) = \begin{cases} \sigma^{n_1} & (\alpha\sigma < 0.8) \\ \exp(\beta\sigma) & (\alpha\sigma > 0.8) \\ [\sin(\alpha\sigma)]^n & (\text{for all } \sigma) \end{cases} \tag{3}$$

where T is the thermodynamic temperature (K), σ is the flow stress (MPa), Q is the activation energy of

deformation (J/mol), A, n, n_1, α and β are the material parameters. These material parameters can be obtained experimentally by linear fitting.

The stress multiplier (α), is an additional variable which modifies the stress value, by making the plots of $\ln\dot{\varepsilon}$ against $\ln[\sinh(\alpha\sigma)]$ at different temperatures linear and parallel [35]. And it can be calculated from $\alpha=\beta/n_1$, in which β and n_1 are the slopes of σ against $\ln\dot{\varepsilon}$ curve and $\ln\sigma$ against $\ln\dot{\varepsilon}$ curve, respectively. n and A can be obtained from the slope and intercept of $\ln[\sinh(\alpha\sigma)]$ against $\ln Z$ curve, respectively. Q can be obtained by the following equation:

$$Q = R\left\{\frac{\partial \ln\dot{\varepsilon}}{\partial \ln[\sinh(\alpha\sigma)]}\right\}_T \left\{\frac{\partial \ln[\sinh(\alpha\sigma)]}{\partial(1/T)}\right\}_{\dot{\varepsilon}} \tag{4}$$

Taking the strain of 0.1 as an example, all the material parameters are obtained and shown in Table 2.

Repeating the above operations, and the material parameters at different strains can also be obtained. The parameters from the strains of 0.1 to 0.8 at the interval of 0.1 in this study were obtained and shown in Fig. 5. After polynomial fitting, the constitutive model of 2219 Al alloy by SCA is established and shown as follows:

Table 2 Values of material parameters under strain of 0.1

Material parameter	Value
α	0.0092
n	8.83
A	9.94×10^{13}
Q/(J·mol^{-1})	177291.93

$$\begin{cases}\dot{\varepsilon} = A(\varepsilon)\sinh[\alpha(\varepsilon)\sigma]^{n(\varepsilon)}\exp\left[\dfrac{-Q(\varepsilon)}{RT}\right]\\ \alpha(\varepsilon) = B_0 + B_1\varepsilon + B_2\varepsilon^2 + B_3\varepsilon^3 + B_4\varepsilon^4 + B_5\varepsilon^5\\ Q(\varepsilon) = C_0 + C_1\varepsilon + C_2\varepsilon^2 + C_3\varepsilon^3 + C_4\varepsilon^4 + C_5\varepsilon^5\\ A(\varepsilon) = E_0 + E_1\varepsilon + E_2\varepsilon^2 + E_3\varepsilon^3 + E_4\varepsilon^4 + E_5\varepsilon^5 + E_6\varepsilon^6\end{cases} \tag{5}$$

All the coefficients of the polynomial for the material parameters are shown in Table 3. The validation of the constitutive model by SCA will be discussed later.

3.3 Modification of constitutive model

In the previous studies, the material parameters and thermal activation energy were regarded as independent of deformation parameters or just strain dependent. The modification made in this work is that the material

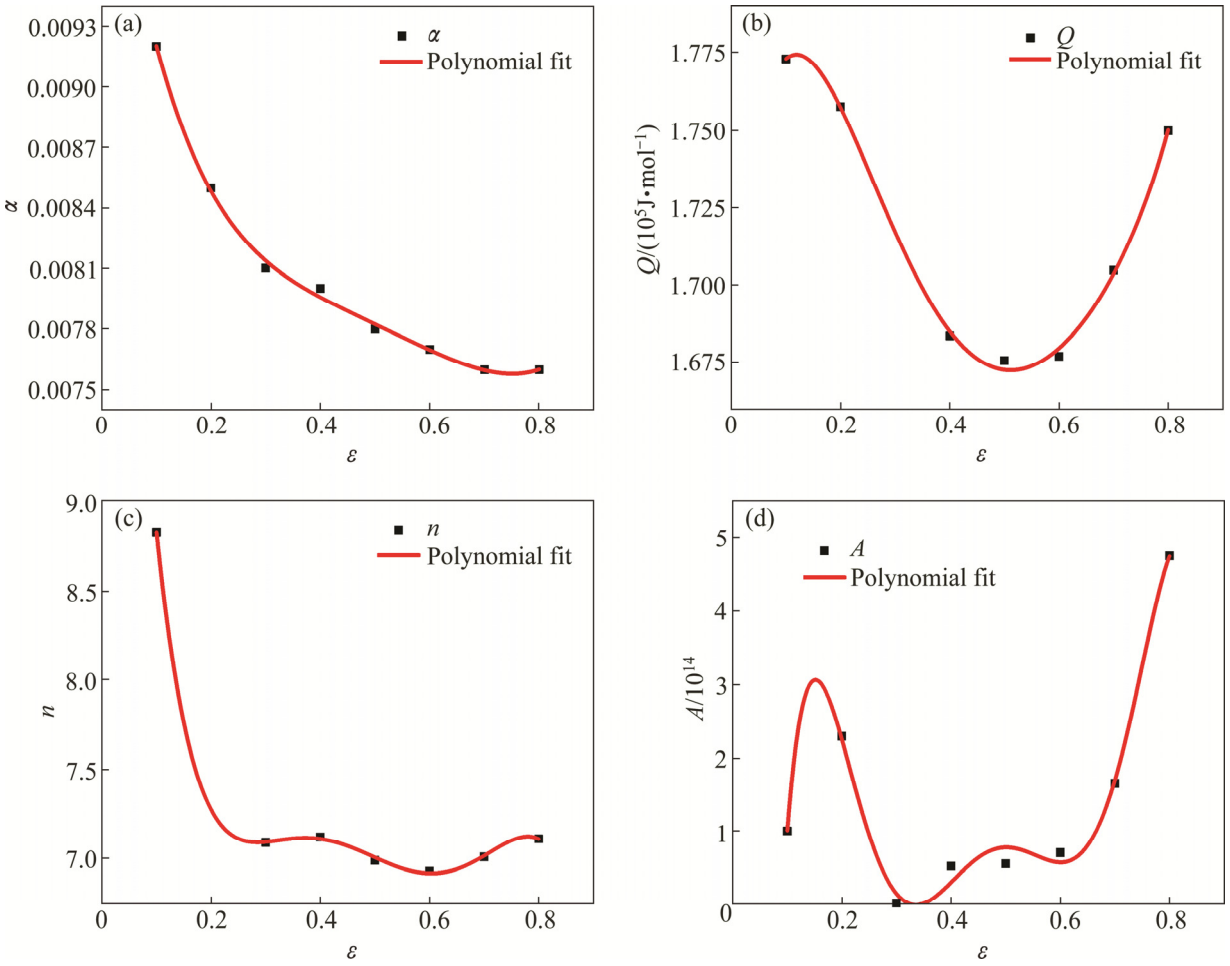

Fig. 5 Relationships between material parameters α (a), Q (b), n (c) and A (d) and true strain ε by polynomial fitting

Table 3 Coefficients of polynomial for material parameters

Parameter	Coefficient value					
	B_0	B_1	B_2	B_3	B_4	B_5
α	0.011	−0.019	0.054	−0.079	0.051	−0.0096
Parameter	Coefficient value					
	C_0	C_1	C_2	C_3	C_4	C_5
Q/(J·mol^{-1})	170008.26	148361.73	−947400.68	2.13×10^6	-2.11×10^6	813365.11
Parameter	Coefficient value					
	D_0	D_1	D_2	D_3	D_4	D_5
n	14.2	−84.83	387.55	−841.86	867.11	−339.93
Parameter	Coefficient value					
	E_0	E_1	E_2	E_3	E_4	E_5	E_6
A	-3.17×10^{16}	6.75×10^{17}	-4.88×10^{17}	1.67×10^{18}	-2.94×10^{18}	2.59×10^{18}	-8.96×10^{17}

parameters are dependent on the deformation parameters. So, the material parameters and thermal activation energy are assumed to be functions of the deformation parameters [36]. That is, A, n, α and Q in Eq. (5) also become material variables. Therefore, Eq. (5) can be rewritten as follows:

$$\dot{\varepsilon} = A(\varepsilon,\dot{\varepsilon},T)\sinh[\alpha(\varepsilon,T)\sigma]^{n(\varepsilon,T)}\exp\left[\frac{-Q(\varepsilon,\dot{\varepsilon},T)}{RT}\right] \quad (6)$$

where α and n are the functions of strain and temperature, Q and A are the functions of strain, strain rate, and temperature. These material variables can be obtained experimentally by nonlinear surface fitting.

3.3.1 Determination of $\alpha(\varepsilon, T)$

The values of α under different temperatures and strains can be obtained as shown in Fig. 6(a).

From Fig. 6(a), it can be clearly seen that the stress multiplier α increases from 0.0055 to 0.01 with the increase in temperature from 483 to 573 K, while the effect of strain is not apparent. The curved surface was used to describe the relationship among the multiplier α, the strain, and temperature as shown in Fig. 6(b). In general, the degree of accuracy of the model can be expressed by the correlation coefficient (R^2) as follows [37]:

$$R^2 = \frac{\sum_{i=1}^{n}(E_i-\overline{E})(F_i-\overline{F})}{\sqrt{\sum_{i=1}^{n}(E_i-\overline{E})^2\sum_{i=1}^{n}(F_i-\overline{F})^2}} \quad (7)$$

where E_i and F_i are the experimental and the predicted values, respectively, $\overline{E}$ and $\overline{F}$ are the means of the experimental and the predicted values under all conditions, respectively. According to the data analysis, the correlation coefficient R^2=0.990, this justified the accuracy of the data obtained as shown in Fig. 6(b). Thus, it is mathematically described below:

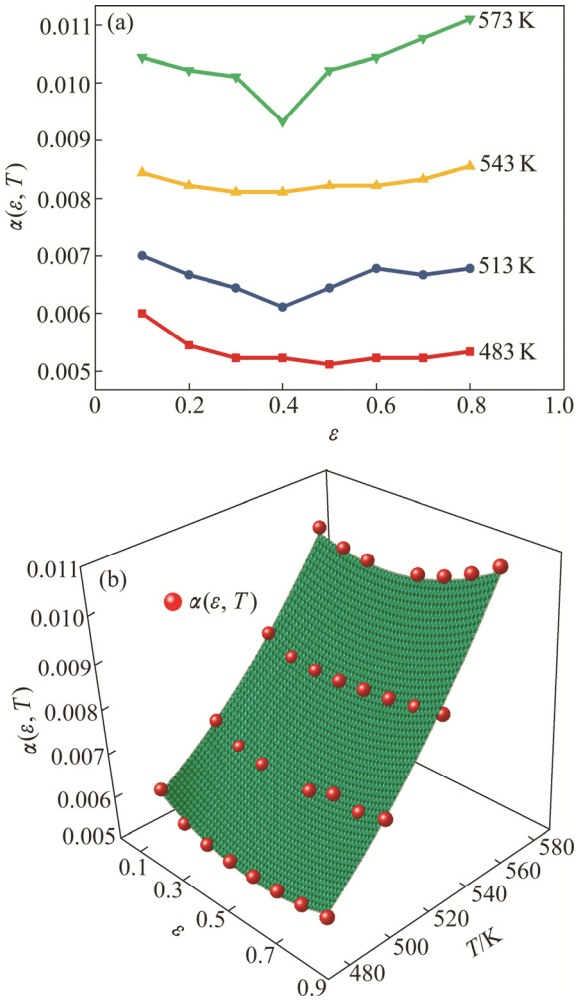

Fig. 6 Variation of stress multiplier $\alpha(\varepsilon, T)$ at different temperatures and strains (a) and 3D illustration of $\alpha(\varepsilon, T)$ and curved surface regression fit (b)

$$\alpha(\varepsilon,T) = 0.0398-0.0123\varepsilon-1.629\times10^{-4}T+0.00426\varepsilon^2+ 1.946\times10^{-7}T^2+1.628\times10-5\varepsilon T \quad (8)$$

3.3.2 Determination of $n(\varepsilon, T)$

Taking the natural logarithm of both sides of Eq. (6) and simplifying result in the following equation:

$$\ln\dot{\varepsilon}=\left[\frac{-Q(\varepsilon,\dot{\varepsilon},T)}{RT}+\ln A(\varepsilon,\dot{\varepsilon},T)\right]+ n(\varepsilon,T)\ln\{\sinh[\alpha(\varepsilon,T)\sigma]\} \quad (9)$$

Therefore, $n(\varepsilon,T)$ can be obtained from the curve slope of $\ln\dot{\varepsilon}$ against $\ln[\sinh[\alpha(\varepsilon,T)\sigma]]$ at different temperatures and strains, and the values are shown in Fig. 7(a).

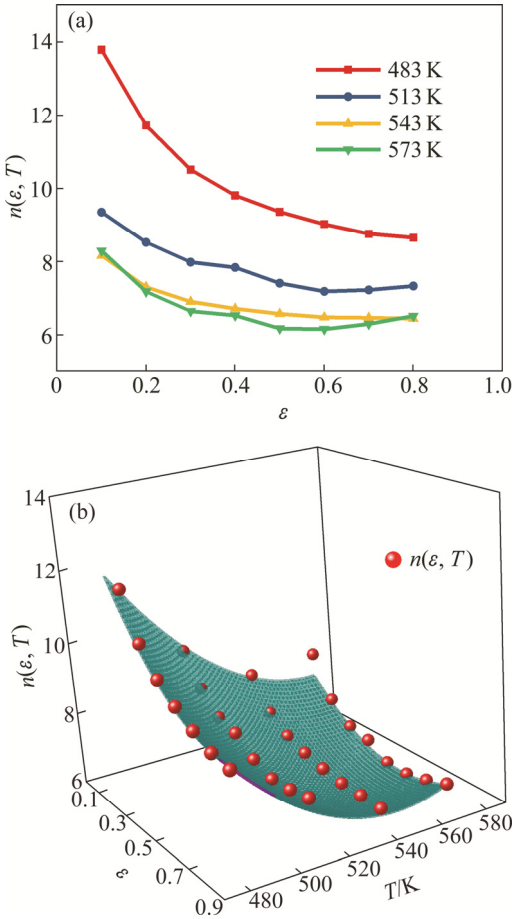

Fig. 7 Variation of $n(\varepsilon, T)$ at different temperatures and strains (a) and 3D illustration of $n(\varepsilon, T)$ and curved surface fitting (b)

As shown in Fig. 7(a), $n(\varepsilon,T)$ decreases significantly with the increase in temperature but keeps almost unchanged above the temperature of 543 K. At a constant temperature, $n(\varepsilon,T)$ decreases with the increase in strain. So, it can be clearly seen that n is very sensitive to temperature and strain. Therefore, n is considered to be a function of temperature and strain as shown in Fig. 7(b). The nonlinear 3D surface fitting of $n(\varepsilon,T)$ at different temperatures and strains has the correlation coefficient R^2=0.974. Thus, the mathematical relation for $n(\varepsilon,T)$ can be expressed as follows:

$$n(\varepsilon,T)=188.42508-25.93864\varepsilon-0.62712T+ 6.87263\varepsilon^2+5.46498\times10^{-4}T^2+0.03161\varepsilon T \quad (10)$$

3.3.3 Determination of $Q(\varepsilon,\dot{\varepsilon},T)$

For a specified strain and strain rate, Eq. (9) can be rewritten as

$$\frac{Q(\varepsilon,\dot{\varepsilon},T)}{Rn(\varepsilon,T)}\cdot\frac{1}{T}=\frac{\ln A(\varepsilon,\dot{\varepsilon},T)-\ln\varepsilon}{n(\varepsilon,T)}+\ln\{\sinh[\alpha(\varepsilon,T)\sigma]\} \quad (11)$$

Therefore, the activation energy can be obtained from the slope of $\ln\{\sinh[\alpha(\varepsilon,T)\sigma]\}$ against $1/T$ curve.

$$Q(\varepsilon,\dot{\varepsilon},T)=1000Rn(\varepsilon,T)\left\{\frac{\partial\ln\{\sinh[\alpha(\varepsilon,T)\sigma]\}}{\partial(1000/T)}\right\}_{\varepsilon,\dot{\varepsilon}} =1000Rn(\varepsilon,T)M(\varepsilon,\dot{\varepsilon}) \quad (12)$$

Equation (12) shows that Q consists of two separate parts: $n(\varepsilon,T)$ and $M(\varepsilon,\dot{\varepsilon})$. $n(\varepsilon,T)$ is a function of strain and temperature, which has been obtained previously, and $M(\varepsilon,\dot{\varepsilon})$ is a function of strain and strain rate, which can be obtained from the slope of $\ln\{\sinh[\alpha(\varepsilon,T)\sigma]\}$ against $1000/T$ curve. Considering that $\alpha(\varepsilon,T)$ itself is dependent on temperature, $\alpha(\varepsilon,T)$ is determined to be the mean value under different temperatures to ensure the linear relationship between them. It has been proved that they have good linear relationship at different strains and strain rates. Figure 8 shows the linear relationship under a strain of 0.6.

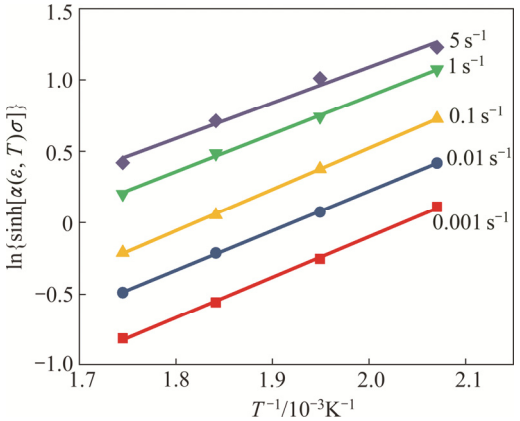

Fig. 8 Relationships between $\ln\{\sinh[\alpha(\varepsilon,T)\sigma]\}$ and $1000/T$ at strain of 0.6 and different strain rates

The slopes at different strains and strain rates, which are also known as $M(\varepsilon,\dot{\varepsilon})$, have been calculated and displayed in Fig. 9(a). It can be seen that $M(\varepsilon,\dot{\varepsilon})$ increases with the increase in strain and decreases with the increase in strain rate. In other words, $M(\varepsilon,\dot{\varepsilon})$ is dependent on strain and strain rate, so $M(\varepsilon,\dot{\varepsilon})$ is considered as a function of strain and the natural logarithm of strain rate in this work. The 3D surface fitting of $M(\varepsilon,\dot{\varepsilon})$ is shown in Fig. 9(b). The correlation coefficient was determined to be R^2=0.933. So, $M(\varepsilon,\dot{\varepsilon})$ can be expressed as follows:

$$M(\varepsilon,\dot{\varepsilon})=1.82345+1.93485\varepsilon-0.14507\ln\dot{\varepsilon}- 0.83007\varepsilon^2-0.00898(\ln\varepsilon)^2+0.11338\varepsilon\ln\dot{\varepsilon} \quad (13)$$

Therefore, the activation energy can be obtained by substituting $n(\varepsilon,T)$ and $M(\varepsilon,\dot{\varepsilon})$ from Eqs. (10) and (13) respectively into Eq. (12).

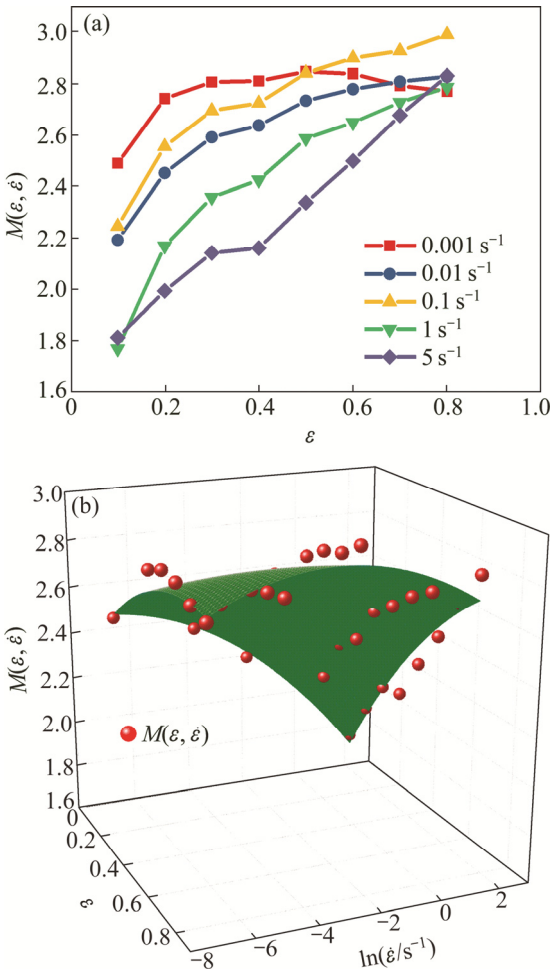

Fig. 9 Variation of $M(\varepsilon,\dot{\varepsilon})$ at different strains and strain rates (a) and 3D illustration of $M(\varepsilon,\dot{\varepsilon})$ and curved surface fitting

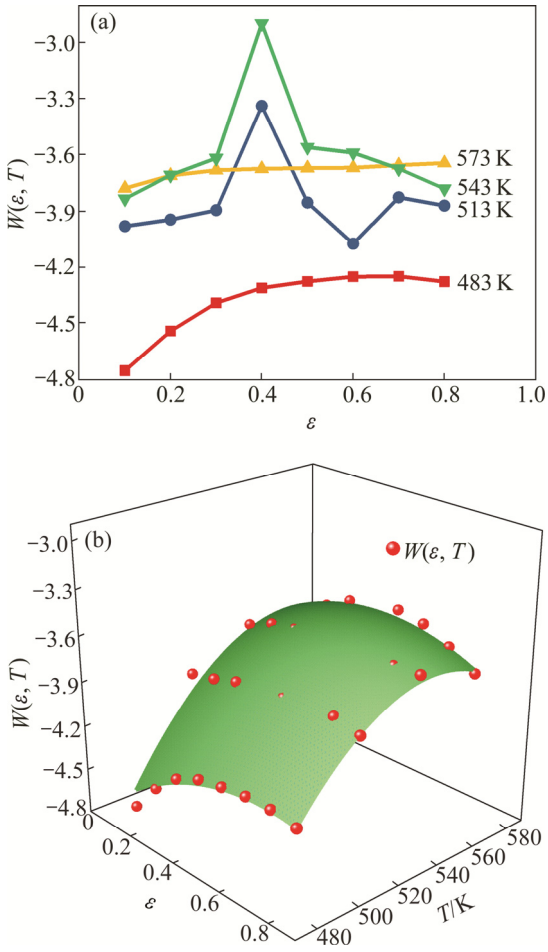

Fig. 10 Variation of $W(\varepsilon,\dot{\varepsilon})$ at different strains and temperatures (a) and 3D illustration of $W(\varepsilon,\dot{\varepsilon})$ and curved surface fitting (b)

3.3.4 Determination of $A(\varepsilon,\dot{\varepsilon},T)$

According to Eq. (9), $[\ln A(\varepsilon,\dot{\varepsilon},T)-Q(\varepsilon,\dot{\varepsilon},T)/(RT)]$ can be obtained from the intercepts of $\ln\{\sinh[\alpha(\varepsilon,T)\sigma]\}$ against $\ln\dot{\varepsilon}$ curves under different temperatures and strains, and recorded as $W(\varepsilon,T)$. The variation of $W(\varepsilon,T)$ at different strains and temperatures is calculated and shown in Fig. 10(a). $W(\varepsilon,T)$ is very sensitive to strain and temperature, so it is written as a function of temperature and strain. The 3D surface fitting of $W(\varepsilon,T)$ is shown in Fig. 10(b). The correlation coefficient R^2=0.972 is employed. Therefore, its mathematical expression can be written as follows:

$$W(\varepsilon,T)=-47.32577+4.27287\varepsilon+0.15389T-1.175831\varepsilon^2-1.35831\times10^{-4}T^2-0.00559\varepsilon T \quad (14)$$

By substituting $Q(\varepsilon,\dot{\varepsilon},T)$ from Eq. (12) into $[\ln A(\varepsilon,\dot{\varepsilon},T)-Q(\varepsilon,\dot{\varepsilon},T)/(RT)]$, the following equation is derived:

$$\ln A(\varepsilon,\dot{\varepsilon},T)=W(\varepsilon,T)+\frac{1000n(\varepsilon,T)M(\varepsilon,\dot{\varepsilon})}{T} \quad (15)$$

3.3.5 Modified constitutive model of 2219 Al alloy

According to the previous calculations, the flow behavior of the 2219 Al alloy during warm deformation can be expressed in temperature range of 483−573 K, strain rate range of 10^{-3}−5 s^{-1} and strain range of 0−0.8 via the following equations:

$$\begin{cases}\sigma=\dfrac{1}{\alpha(\varepsilon,T)}\sinh^{-1}\left\{\dfrac{\dot{\varepsilon}\exp[Q(\varepsilon,\dot{\varepsilon},T)/(RT)]}{A(\varepsilon,\dot{\varepsilon},T)}\right\}^{1/n(\varepsilon,T)}\\ n(\varepsilon,T)=188.42508-25.93864\varepsilon-0.62712T+6.87263\varepsilon^2+5.46498\times10^{-4}T^2+0.03161\varepsilon T\\ Q(\varepsilon,\dot{\varepsilon},T)=1000Rn(\varepsilon,T)M(\varepsilon,\dot{\varepsilon})\\ M(\varepsilon,\dot{\varepsilon})=1.82345+1.93485\varepsilon-0.14507\ln\dot{\varepsilon}-0.83007\varepsilon^2-0.00898(\ln\dot{\varepsilon})^2+0.11338\varepsilon\ln\dot{\varepsilon}\\ \ln A(\varepsilon,\dot{\varepsilon},T)=W(\varepsilon,T)+\dfrac{1000n(\varepsilon,T)M(\varepsilon,\dot{\varepsilon})}{T}\\ W(\varepsilon,T)=-47.32577+4.27287\varepsilon+0.15369T-1.17518\varepsilon^2-1.35831\times10^{-4}T^2-0.00559\varepsilon T\end{cases} \quad (16)$$

3.4 Verification of conventional model by SCA and modified model

A good constitutive model not only depends on the degree of fitting to the modeling data used, but also is capable of making accurate predictions under the limited deformation conditions. Therefore, both the modeling and prediction sets should be verified using the conventional model by SCA and the modified model, respectively. The comparison between the computational stresses calculated by Eqs. (5) and (16) and the experimental stresses under different deformation conditions are shown in Fig. 11. It can be observed that the calculated stresses obtained from the modified model are in good agreement with the experimental values. However, the calculated stresses by the conventional model exhibit noticeable deviation from the experimental values in both modeling and prediction set.

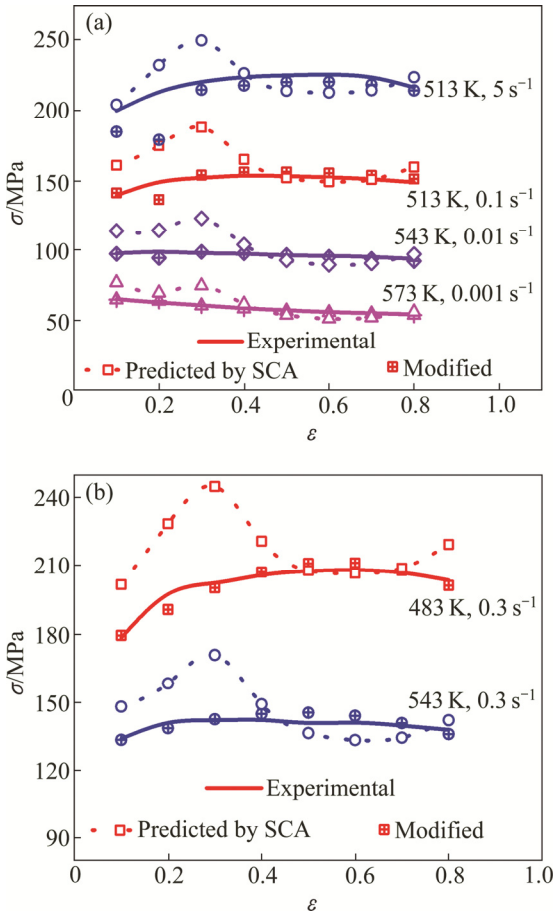

Fig. 11 Comparisons between predicted by SCA, modified and experimental flow stresses of 2219 Al alloy for modeling set (a) and prediction set (b)

Also, to quantitatively assess the accuracy of the model, the correlation coefficients (R^2) and the average relative error (AARE) parameters (as shown in Eq. (17)) of the two models are calculated respectively and illustrated in Fig. 12. The results show that the correlation coefficient is 0.994, and *AARE* is 2.12% as obtained from the modified model. But, the correlation coefficient is only 0.932, and *AARE* is 9.00% based on the conventional model. This fully demonstrates that the modified constitutive model has better performance in both modeling and prediction than the conventional model by SCA.

$$AARE=\frac{1}{N}\sum_{i=1}^{N}\left|\frac{\sigma_{ex}^{i}-\sigma_{p}^{i}}{\sigma_{ex}^{i}}\right|\times 100\% \tag{17}$$

where σ_{ex} is the experimental flow stress, σ_p is the computational stress calculated by the constitutive model, N is the total number of the experimental data.

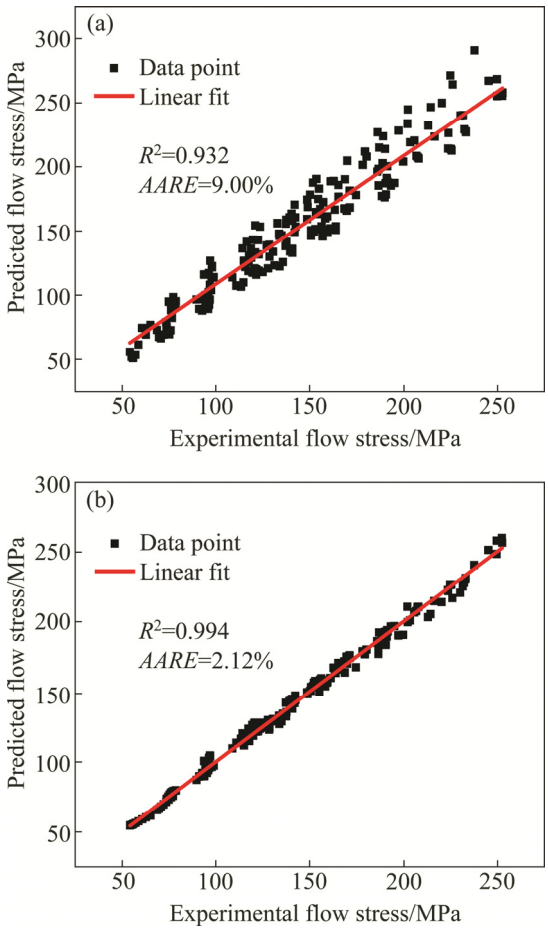

Fig. 12 Correlation between experimental and calculated flow stresses by obtained conventional model by SCA (a) and modified constitutive model (b)

Conclusively, the modified constitutive model considering deformation parameters can be used to simulate the flow behavior of 2219 Al alloy during warm deformation.

3.5 Evolution of activation energy

The activation energy can be calculated using the modified constitutive model (Eq. (16)) under different deformation conditions. The charts of the activation

energy against temperature and strain rate were obtained under different strains respectively; the results are shown in Fig. 13.

It can be clearly seen from Fig. 13 that the activation energy varies significantly at different temperatures, strain rates and strains in the range from 121.5 to 266 kJ/mol. Further, it is found that the activation energy decreases with the increase in temperature and strain rate. This is related to the thermodynamic mechanism of the dislocation motion. Plastic deformation of Al alloy is mainly due to the slip of dislocation on slip surface. When the energy barrier (activation energy) can be overcome, the dislocation can be moved randomly, which is a thermal activation process. In addition, the energy barrier can be overcome when the external shear stress on the sliding surface is more than the Peierls−Nabarro stress, and then the dislocation can be moved freely [38].

The activation energy decreases with the increase in temperature, this is due to the beneficial effect to overcome the barriers of dislocation movement at high temperature. Specifically, dislocations can move with higher kinetic energy when the temperature is increased, and also it makes the deformation much easier. Moreover, the dynamic recovery is strengthened, and the dislocation density is decreased with the increase in temperature, which is also beneficial to the dislocation movement. Therefore, it can effectively reduce the resistance of the dislocation movement and the thermal activation energy by increasing the deformation temperature.

On the other hand, the applied external force will increase with the increase in strain rate, which will increase the shear stress to activate the dislocation movement. Furthermore, the multiplication rate of dislocation will increase with the increase in strain rate, which is beneficial to the occurrence of dynamic recovery, thus promoting the dislocation movement. However, the increase in strain rate can also result in the entanglement of dislocation structures and incomplete dynamic recovery due to the shorter deformation time. That is to say, the first two factors can reduce the thermal activation energy and facilitate plastic deformation, whereas the other two factors play the opposite role. This experiment proves that the first two factors play a major role in the warm deformation process so that thermal activation decreases with the increase in strain rate.

The effect of strain on the thermal activation energy is shown in Fig. 14. It can be observed that the effect of strain on the thermal activation energy is coupled with the effect of strain rate. In the case of low strain rate

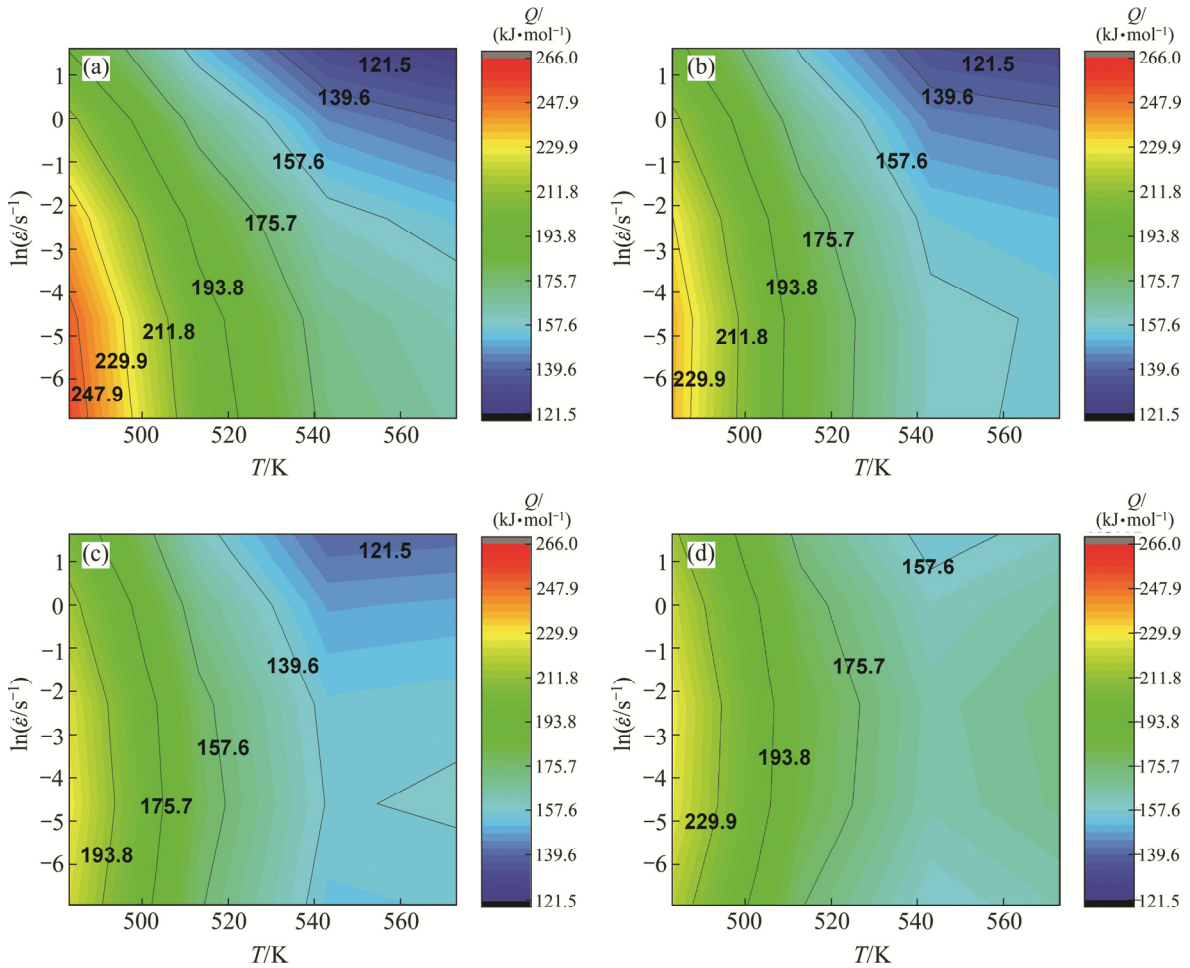

Fig. 13 Evolution of activation energy under different strains: (a) 0.2; (b) 0.4; (c) 0.6; (d) 0.8

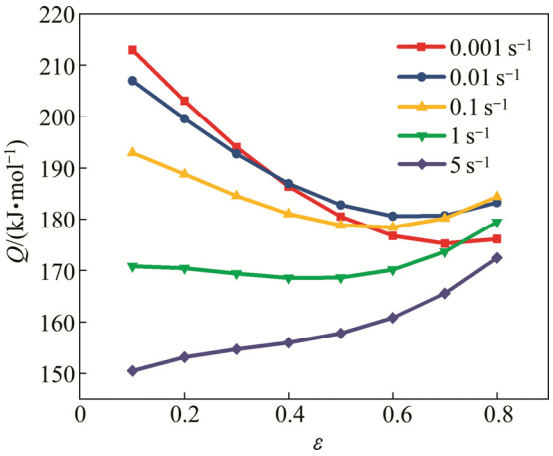

Fig. 14 Relationship between activation energy and true strain at 513 K

(<1 s^{-1}), the activation energy reduces with the increase in strain, while in the case of high strain rate (>1 s^{-1}), the activation energy increases with the increase in strain. This is because the activation time of dislocation is prolonged at a lower strain rate, and the dynamic recovery process can be fully carried out by increasing the amount of deformation. This makes the activation energy gradually decrease with the increase in strain. While at the high strain rate, the tangled dislocation structures become severer with the increase in strain, which is not conducive to further dislocation movement, thus resulting in the increase in activation energy.

4 Conclusions

(1) The flow stress of 2219 Al alloy is very sensitive to deformation temperature and strain rate, and it increases with the decrease in temperature or the increase in strain rate. The softening mechanism of 2219 Al alloy during warm deformation is mainly dynamic recovery.

(2) Considering the activation energy and material parameters as variables of deformation parameters, a modified hyperbolic sine constitutive model of 2219 Al alloy is established, and the flow behaviors are predicted with R^2=0.994 and *AARE*=2.12%.

(3) The evolution of the activation energy indicates that the deformation process is a thermal activation process, which is affected by temperature, strain rate, and strain. The range of activation energy obtained is 121.5−266 kJ/mol. Furthermore, it decreases with the increase in temperature and strain rate, and it is also influenced by the coupled effect of strain and strain rate.

References

[1] LEQUEU P, LASSINCE P, WARNER T. Al alloy development for the Airbus A380: Part 2 [J]. Advanced Materials & Processes, 2007, 165(7): 41−44.

[2] KAIBYSHEV R, SITDIKOV O, MAZURINA I. Deformation behavior of a 2219 Al alloy [J]. Materials Science & Engineering A, 2002, 334(1):104−113.

[3] LUO C H, PENG W P, CHEN T. Influence of heat treatment on properties of 2219AA-T6 FSW joints [J]. Applied Mechanics & Materials, 2014, 590: 187−191.

[4] YANG Y, ZHAN L, SHEN R. Effect of pre-deformation on creep age forming of 2219 Al alloy: Experimental and constitutive modelling [J]. Materials Science & Engineering A, 2017, 683: 227−235.

[5] PANIGRAHI S K, JAYAGANTHAN R, PANCHOLI V. Effect of plastic deformation conditions on microstructural characteristics and mechanical properties of Al 6063 alloy [J]. Materials & Design, 2009, 30(6): 1894−1901.

[6] JI H S, JI H K, WAGONER R H. A plastic constitutive equation incorporating strain, strain-rate, and temperature [J]. International Journal of Plasticity, 2010, 26(12): 1746−1771.

[7] SELLARS C M, MCTEGART W J. On the mechanism of hot deformation [J]. Acta Metallurgica, 1966, 14(9): 1136−1138.

[8] CEPEDA-JIMÉNEZ C M, RUANO O A, CARSÍ M. Study of hot deformation of an Al−Cu−Mg alloy using processing maps and microstructural characterization [J]. Materials Science & Engineering A, 2012, 552(9): 530−539.

[9] TRIMBLE D, O'DONNELL G E. Flow stress prediction for hot deformation processing of 2024Al-T3 alloy [J]. Transactions of Nonferrous Metals Society of China, 2016, 26(5): 1232−1250.

[10] LIN Y C, CHEN M S, ZHANG J. Modeling of flow stress of 42CrMo steel under hot compression [J]. Materials Science & Engineering A, 2009, 499(1−2): 88−92.

[11] XIAO Y H, GUO C, GUO X Y. Constitutive modeling of hot deformation behavior of H62 brass [J]. Materials Science & Engineering A, 2011, 528(21): 6510−6518.

[12] MHGHAVAM, MMORAKABATI, SMABBASI. Flow behavior modeling of IMI834 titanium alloy during hot tensile deformation [J]. Transactions of Nonferrous Metals Society of China, 2015, 25(3): 748−758.

[13] MALLOL J, SARRAGA MC, BARTOLOMÉ M. Hot working behavior of near-α alloy IMI834 [J]. Materials Science & Engineering A, 2005, 396(1−2): 50−60.

[14] HAGHDADI N, ZAREI-HANZAKI A, ABEDI H R. The flow behavior modeling of cast A356 Al alloy at elevated temperatures considering the effect of strain [J]. Materials Science & Engineering A, 2012, 535(7): 252−257.

[15] ROKNI M R, ZAREI-HANZAKI A, ROOSTAEI A. Constitutive base analysis of a 7075-Al alloy during hot compression testing [J]. Materials & Design, 2011, 32(10): 4955−4960.

[16] LIN Y C, CHEN X M, WEN D X. A physically-based constitutive model for a typical nickel-based superalloy [J]. Computational Materials Science, 2014, 83(2): 282−289.

[17] LIN Y C, LI Q F, XIA Y C. A phenomenological constitutive model for high temperature flow stress prediction of Al−Cu−Mg alloy [J]. Materials Science & Engineering A, 2012, 534(1): 654−662.

[18] LIN Y C, LI L T, JIANG Y Q. A Phenomenological constitutive model for describing thermo-viscoplastic behavior of Al−Zn−Mg−Cu alloy under hot working condition [J]. Experimental Mechanics, 2012, 52(8): 993−1002.

[19] QUAN G Z, YU C T, LIU Y. A Comparative study on improved Arrhenius-type and artificial neural network models to predict high-temperature flow behaviors in 20MnNiMo alloy [J]. Scientific World Journal, 2014, 2014(1): 108492.

[20] QUAN G Z, WANG T, LI Y L. Artificial neural network modeling to evaluate the dynamic flow stress of 7050 Al alloy [J]. Journal of Materials Engineering & Performance, 2016, 25(2): 1−12.

[21] QUAN G Z, LV W Q, MAO Y P. Prediction of flow stress in a wide

temperature range involving phase transformation for as-cast Ti−6Al−2Zr−1Mo−1V alloy by artificial neural network [J]. Materials & Design, 2013, 50(17): 51−61.

[22] ZHANG W F, SHA W, YAN W, WANG W, SHAN Y Y. Analysis of deformation behavior and workability of advanced 9Cr−Nb−V ferritic heat resistant steels [J]. Materials Science & Engineering A, 2014, 604: 207−214.

[23] SAMANTARAY D, MANDAL S, BHADURI A K. A comparative study on Johnson Cook, modified Zerilli–Armstrong and Arrhenius-type constitutive models to predict elevated temperature flow behaviour in modified 9Cr−1Mo steel [J]. Computational Materials Science, 2009, 47(2): 568−576.

[24] ZHANG W F, SHA W, YAN W. Constitutive modeling, microstructure evolution, and processing map for a nitride-strengthened heat-resistant steel [J]. Journal of Materials Engineering & Performance, 2014, 23(8): 3042−3050.

[25] KAIBYSHEV R, SITDIKOV O, MAZURINA I. Deformation behavior of a 2219 Al alloy [J]. Materials Science & Engineering A, 2002, 334(1): 104−113.

[26] WARD B R, AGRAWAL S P, ASHTON R F. Method of producing superplastic Al sheet: US patent, 4486244 A [P]. 1984−12−04.

[27] TOROS S, OZTURK F, KACAR I. Review of warm forming of Al–magnesium alloys [J]. Journal of Materials Processing Technology, 2008, 207(1−3): 1−12.

[28] LI D, GHOSH A K. Biaxial warm forming behavior of Al sheet alloys [J]. Journal of Materials Processing Technology, 2004, 145(3): 281−293.

[29] WANG C, YU F, ZHAO D. Hot deformation and processing maps of DC cast Al−15%Si alloy [J]. Materials Science & Engineering A, 2013, 577(11): 73−80.

[30] WEI H L, LIU G Q, ZHANG M H. Physically based constitutive analysis to predict flow stress of medium carbon and vanadium microalloyed steels [J]. Materials Science & Engineering A, 2014, 602: 127−133.

[31] DEVADAS C, BARAGAR D, RUDDLE G. The thermal and metallurgical state of steel strip during hot rolling: Part II. Factors influencing rolling loads [J]. Metallurgical Transactions A, 1991, 22(2): 321.

[32] BARAGAR D L. The high temperature and high strain-rate behaviour of a plain carbon and an HSLA steel [J]. Journal of Mechanical Working Technology, 1987, 14(3): 295−307.

[33] DONG Y, ZHANG C, ZHAO G. Constitutive equation and processing maps of an Al−Mg−Si Al alloy: Determination and application in simulating extrusion process of complex profiles [J]. Materials & Design, 2016, 92: 983−997.

[34] ASHTIANI H R, SHAHSAVARI P. Strain-dependent constitutive equations to predict high temperature flow behavior of AA2030 Al alloy [J]. Mechanics of Materials, 2016, 100: 209−218.

[35] MCQUEEN H J, RYAN N D. Constitutive analysis in hot working [J]. Materials Science & Engineering A, 2002, 322(1): 43−63.

[36] MOHAMADIZADEH A, ZAREI-HANZAKI A, ABEDI H R. Modified constitutive analysis and activation energy evolution of a low-density steel considering the effects of deformation parameters [J]. Mechanics of Materials, 2016, 95: 60−70.

[37] SHAMSOLHODAEI A, ZAREI-HANZAKI A, GHAMBARI M. The high temperature flow behavior modeling of NiTi shape memory alloy employing phenomenological and physical based constitutive models: A comparative study [J]. Intermetallics, 2014, 53(11): 140−149.

[38] MORISHIGE K, KITTAKA S, MORIMOTO T. The plastic deformation of metals [J]. Bulletin of the Chemical Society of Japan, 1980, 53(8): 2128−2132.

2219 铝合金中温变形过程本构模型的修正及其激活能演化

刘 磊[1,2,3]，吴运新[1,2,3]，龚 海[1,2,3]，王 凯[1,2,3]

1. 中南大学 轻合金研究院，长沙 410083；
2. 中南大学 有色金属先进结构材料与制造协同创新中心，长沙 410083；
3. 中南大学 高性能复杂制造国家重点实验室，长沙 410083

摘 要：为了研究 2219 铝合金的中温流变特性，利用 Gleeble−3500 热压缩实验机，在不同温度(483~573 K)及应变速率(0.001~5 s^{-1})的条件下进行热压缩实验。实验获得的真应力−真应变曲线表明，流变应力随着温度的降低和/或应变速率的升高而增大，且变形过程中的软化机制主要是动态回复。然后，基于材料变量和激活能对形变参数的依赖性，对传统的 Arrhenius 型本构模型进行参数修正。经验证，所建立修正的本构模型能很好地预测 2219 铝合金在中温变形条件下的流变应力。另外，基于此修正模型获得不同条件下的热激活能。激活能随温度和/或应变速率的升高而降低，且受应变和应变速率的耦合作用影响。

关键词：2219 铝合金；中温变形；流变行为；本构模型；激活能

(Edited by Wei-ping CHEN)